A&A, 711, A201 (2026)
https://doi.org/10.1051/0004-6361/202557010

Astronomy & Astrophysics

Multi-map holography for large crossed-Dragone telescopes

X. Ren[1,6,⋆], R. E. Hills[2,⋆⋆], U. U. Graf[1], B. Nikolic[2], N. Reyes[3,5], L. Graf[1], P. Astudillo[4,8], S. Jorquera[4,7], and R. Puddu[7]

[1] I. Physikalisches Institut, Universität zu Köln, Zülpicher Straße 77, 50937 Köln, Germany
[2] Cavendish Laboratory, University of Cambridge, Cambridge CB3 0HE, UK
[3] Max Planck Institute for Radio Astronomy, Bonn, Germany
[4] Departamento de Astronomía, Universidad de Chile, Santiago 7591245, Chile
[5] Departamento de Ingeniería Eléctrica, Universidad de Chile, Santiago 8370451, Chile
[6] School of Engineering and Natural Sciences, University of Iceland, 107 Reykjavík, Iceland
[7] Instituto de Astrofísica and Centro de Astro-Ingeniería, Facultad de Física, Pontificia Universidad Católica de Chile, Santiago, Chile
[8] National Radio Astronomy Observatory, Central Development Laboratory, Charlottesville, VA 22903 USA

Received 27 August 2025 / Accepted 8 June 2026

ABSTRACT

We present a novel microwave holography technique for large crossed-Dragone telescopes, which feature two similarly sized off-axis reflectors whose surface deformations must be measured and corrected independently. A major challenge in these systems is the degeneracy of wavefront distortions caused by surface errors on both reflectors, which conventional single-beam holography cannot effectively disentangle. The method addresses this challenge by acquiring five beam maps at distinct focal plane positions and employing an inference-based analysis to reconstruct the individual surface error distributions of the two large reflectors. We developed a fast and accurate beam analysis method based on the Fresnel-Kirchhoff diffraction theorem to accelerate the forward beam calculations. This greatly reduces the computational cost while maintaining high accuracy, enabling a practical application to iterative fittings for the large crossed-Dragone telescopes. The accuracy and feasibility of the new technique have been verified by numerical simulations for the FYST telescope and experimental tests for a 400 mm diameter crossed-Dragone optics.

Key words. methods: analytical – methods: numerical – site testing – space vehicles: instruments – telescopes

1. Introduction

Large reflectors in telescopes operating at millimeter and submillimeter wavelengths are typically segmented into smaller panels to facilitate manufacturing and alignment. These panels are fabricated with high precision, mounted onto a backup structure, and carefully aligned to meet the required surface accuracy across the entire reflector. Deviations of the reflector surfaces from their designed profiles introduce phase errors across the telescope aperture, thereby reducing the aperture efficiency. This effect is commonly described by the phase-error efficiency, η_ϕ (Milligan 2005, Chap. 8). For random reflector surface errors, Ruze's analysis (Ruze 1966) gives

$$\eta_\phi \approx \exp\left[-\left(\frac{4\pi\sigma}{\lambda}\right)^2\right], \tag{1}$$

where σ is the root mean square (rms) surface deviation and λ is the observing wavelength. A practical rule of thumb is that the rms surface error should remain below about one-sixteenth of the shortest operating wavelength, at which the phase-error efficiency is already reduced to about 50%. In addition to reducing the phase-error efficiency, surface deviations also increase the telescope response in the error beams, thereby enhancing susceptibility to stray light and degrading the telescope sensitivity. Therefore, accurately measuring and correcting surface deformations due to panel misalignment becomes critical to preserving the electromagnetic performance of the telescope across its full operating band. In particular, for telescopes operating at submillimeter wavelengths, the shorter wavelength makes the beam quality much more sensitive to reflector deformations, so a given level of surface error causes substantially greater degradation.

Millimeter and submillimeter telescopes are commonly built at very high-altitude sites to minimize atmospheric absorption and access short-wavelength atmospheric windows. These conditions enable a broad range of science. Examples include probing star formation in the Milky Way and nearby galaxies through observations of molecular and fine-structure lines, such as spectral lines of atomic carbon and carbon monoxide, tracing the evolution of dusty star-forming galaxies across cosmic time, and studying galaxies and galaxy-cluster formation through the Sunyaev–Zel'dovich effect on the cosmic microwave background (CMB; CCAT-Prime Collaboration 2022; Ramasawmy et al. 2022). Many of the targeted line signals, especially those from distant or diffuse sources, are faint. Realizing these science goals therefore requires high sensitivity, high aperture efficiency, and good beam fidelity across the full operating band. In turn, this places stringent requirements on the reflector surface accuracy.

Microwave holography (Bennett et al. 1976; Scott & Ryle 1977) has been proven to be an efficient and accurate method to measure the surface errors of the reflectors of large antennas and is widely adopted by modern radio telescopes. This technique relies on the Fourier transform relationship between

⋆ Corresponding author: ren@ph1.uni-koeln.de
⋆⋆ Deceased: June 2022. This work is dedicated to his memory.

the telescope's complex far-field beam map and its complex aperture field (Silver 1984). If the complex far-field beam map of the telescope is measured, the corresponding aperture field can be reconstructed by making an inverse Fourier transform (FT) of the measured beam pattern. The surface distortions of the reflector are then deduced from the phase distribution of the reconstructed aperture field using geometric projection. For high surface accuracy measurements, such as those for telescopes designed to operate at submillimeter wavelengths where surface precision is required to be better than tens of microns or even <10 µm, the beam maps are typically measured in the near field using a strong artificial source (Hills et al. 2002; Yaghjian 1986). This ensures a high signal-to-noise ratio (S/N) while minimizing atmospheric effects. However, near-field measurements complicate the analysis: the Fourier transform needs to be replaced by a complex transform, and additional corrections on the measured reflector surface are needed (Baars 2007). This approach has been applied to the alignment of the Atacama Large Millimeter/submillimeter Array (ALMA) prototype antenna, achieving a measurement accuracy of 5 µm (Baars et al. 2007).

Another alternative approach, called phase-retrieval holography (Morris et al. 1988), was developed for cases where only the intensity of the telescope beam pattern can be measured. This method requires measuring power beam maps with the receiver placed at two different axial positions; therefore, it is also known as out-of-focus (OOF) holography (Nikolic et al. 2007a). The advantage of this approach is that it enables the measurement of the reflector deformations at different elevations using astronomical receivers and celestial sources. However, this approach is mainly sensitive to relatively large- and medium-scale surface errors, and has been implemented on 100-m class radio telescopes, including the Green Bank Telescope (Nikolic et al. 2007b) and the Effelsberg 100-m telescope (Cassanelli et al. 2024).

Conventional full-phase holography and phase-retrieval holography usually only provide the error map of the large primary reflector of the telescope, assuming that the errors in the small secondary mirror and errors in the phase pattern of the receiver feed can be neglected or corrected from theory or laboratory measurements. However, in certain specialized telescope designs, such as large crossed-Dragone (CD) optical systems (Dragone 1978; Niemack 2016), the secondary reflector is comparable in size to the primary and must also be segmented into panels and aligned to achieve the required precision. For this optical setup, conventional holography becomes inadequate, as it cannot distinguish which surface errors originate from the primary reflector and which from the secondary. This means that both contributions are degenerate in the measured aperture phase distribution.

In this paper, we present a new holographic method for the CD telescopes, based on measuring beam maps at several positions in the focal plane. The new method employs a numerical fitting technique to reconstruct the reflector shapes by parameterizing both surface deviations and systematic errors present in the measurements. A key contribution of this work is the development of a fast and accurate beam simulation technique for CD optics, enabling efficient analysis and model fitting. The work is motivated by the holographic experiments for the Fred Young Sub-mm Telescope (FYST), which is the largest submillimeter CD telescope. Thus all the simulations shown in this paper are based on the FYST holographic model. But the method is more flexible and can be readily applied to other "two-reflector" systems.

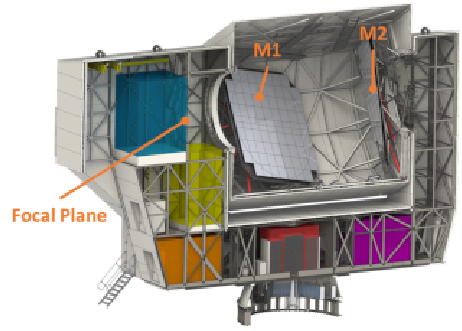

Fig. 1. FYST telescope showing the two segmented reflectors, primary reflector (M1) and secondary reflector (M2), and its focal plane.

FYST is a 6 m coma-corrected CD telescope (Parshley et al. 2018a,b), located at an altitude of 5600 m in the Atacama region of northern Chile. The telescope is designed to operate at frequencies up to 1.5 THz, as the 200-micron atmospheric window is expected to be accessible due to the excellent atmospheric transparency of the high and superbly dry site. This makes possible ground-based observations of far-infrared fine-structure lines such as [N II] 205 µm, a tracer of ionized gas and an important cooling line of the warm ionized medium (Oberst et al. 2006). The advanced CD optics consist of two large reflectors arranged in a cross configuration to provide zero aperture blockage and a very large field of view (FoV), while simultaneously preserving beam symmetry and low cross-polarization. The FoV of FYST is further enhanced to 26 deg^2 at 2 mm wavelength and 4.4 deg^2 at 350 µm by applying additional coma-correction terms on the two reflectors. Both reflectors are approximately 6 meters in diameter and are segmented into 77 panels on the primary reflector (M1) and 69 on the secondary (M2), with panel sizes of 670 × 750 mm and 700 × 710 mm, respectively. Figure 1 illustrates the optical schematic and the cross-sectional view of the FYST telescope.

FYST is a multi-instrument platform equipped with the CCAT Heterodyne Array Instrument (CHAI) and Prime-Cam, enabling a broad range of science programs, from cosmological probes to studies of galaxy evolution across cosmic time (CCAT-Prime Collaboration 2022). Prime-Cam consists of seven independent instrument modules housed in a 1.8-m diameter cryostat, designed to take full advantage of the large field of view provided by the CD optics, and operates over frequencies spanning approximately 200–850 GHz. CHAI is a dual-band, high-resolution spectrometer operating at 460 GHz and 820 GHz (Barrueto et al. 2022). To maintain high beam quality across the entire field of view and preserve the telescope's efficiency up to 1.5 THz, the two reflector surfaces must be aligned with a precision better than 7 µm, resulting in a total effective surface error of about 10 µm. Achieving this requires a surface measurement accuracy better than 3 µm and a spatial resolution of approximately 100 mm, ensuring that measured surface-error maps capture sufficient detail across the ~700 mm panels to be reliably converted into panel-adjuster movements for surface correction and alignment. To achieve this level of accuracy, 300 GHz near-field holography is adopted, with the source mounted about 300 m away from the telescope to minimize atmospheric effect and provide a strong signal. The high observing frequency ensures that a given fractional error in the measured beam pattern is converted into a small error in the reconstructed surface profile. The details of the system design can be found in Ren et al. (2020).

A multi-map holography metrology has been developed to address the degeneracy problem. This approach requires measuring the telescope's beam maps at several well-separated points in the focal plane so that the projections of the surface errors from M1 and M2 onto the aperture plane are sufficiently shifted with respect to each other. This spatial separation allows us to break the degeneracy and separate the surface error maps of the two reflectors. In principle, placing the holographic receiver at three well-separated points and measuring both the amplitude and phase of the telescope beam is sufficient to resolve the degeneracy, but the numerical simulations indicate that using more beam maps improves the accuracy and robustness of the results. For the planned FYST holography measurements, five beam maps will be measured. The maximum separation between the receiver positions is approximately 1130λ at 300 GHz. The corresponding receiver positions and a schematic of the FYST optical configuration are illustrated in Fig. A.1.

Nonetheless, a key limitation remains: there is no straightforward method to directly invert the three or more measured beam maps into the two surface error maps. To address this, the inversion problem can be reformulated as a numerical inference task involving the following steps:

1. The surface deviations are described by a set of parameters. The parameterization must be capable of capturing the surface errors with the required spatial resolution. In addition, systematic errors present in the measurement system are also included as part of the parameterization to ensure a comprehensive and accurate model.
2. A forward model is established to compute the complex beam patterns for a the given set of parameters.
3. A numerical fitting algorithm is employed to determine the set of the surface-parameter values that can best reproduce the measured beam maps. The fitting process typically involves thousands of iterations. Consequently, the accuracy and computational efficiency of the model are critical.

The paper is organized as follows. In Sect. 2, we investigate several strategies for accelerating beam-map simulations. Section 3 details the parameterization of the reflector surfaces and the associated fitting procedure and algorithm. In Sect. 4, the accuracy, sensitivity, and optimal configuration of the multi-map holography method for FYST are investigated via numerical simulations. The feasibility of the proposed method is further validated in Sect. 5 through experimental measurements on a small CD telescope in the laboratory.

2. Beam simulations for crossed-Dragone optics

In practical holographic measurements, a signal originating from a distant source propagates to the telescope aperture, where it is collected by the reflectors and directed to the receiver at the focal plane. To simulate the observed beam maps, it is more convenient to model the equivalent time-reversed process, where the signal starts from the receiver and propagates through the telescope optics to calculate the scattered fields at the distance of the source region. Physical optics (PO) analysis (Rusch & Potter 2013; Collin & Zucker 1969) is a standard approach for modeling the diffraction beam patterns of large reflector antennas. The method can offer high field accuracy and is also computationally efficient when the dimensions of the optical components are not more than a few hundred wavelengths. Implementing the PO analysis for the 6-m FYST holography involves finding the surface currents on M2 excited by the field radiated from the receiver feed, then calculating the fields at the surface of M1

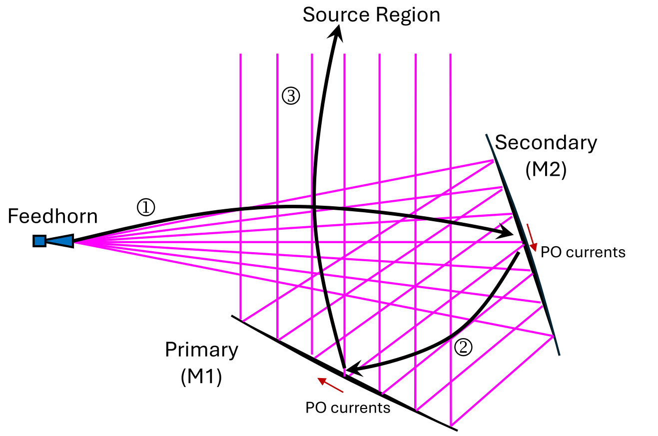

Fig. 2. PO analysis procedure for the FYST beam simulations. The PO analysis follows a time-reversed process. A Gaussian beam produced by the receiver's feed horn illuminates the secondary reflector (M2), inducing surface PO currents (step 1). These currents, in turn, radiate toward the primary reflector (M1), where they induce PO currents on the M1 surface (step 2). Finally, the PO currents on M1 generate the field in the distant source region (step 3).

radiated by those surface currents on M2, and hence finding the induced surface currents on M1, and finally computing the fields radiated by the currents on M1 at the source region. These calculating steps are illustrated in Fig. 2.

Since the FYST holography system operates at 300 GHz, both its reflectors are approximately 6000 wavelengths in diameter. This makes the PO integration highly time-consuming. Moreover, the special optical layout brings the two reflectors very close together, as shown in Fig. 2. This causes M1 to subtend a large angle as seen from M2. As a result, to accurately compute the scattered fields on M1, the induced currents on M2 need to be densely sampled, which makes the simulation more expensive. Nevertheless, we have carried out this laborious PO simulation using a commercial software package, TICRA GRASP, which is the industry-standard software for analyzing reflector antennas based on the PO method and related techniques. It took about 10 days to compute a single beam map at 300 GHz with a field accuracy of −80 dB, using 64 CPU threads. This wall-clock time corresponds to an end-to-end GRASP workflow including auto-convergence testing (repeated runs with sampling refinement until the −80 dB criterion is met). Figure 3 shows the simulated co-polarization and cross-polarization beam patterns of FYST in the near field, where the source is located 300 meters away from the telescope center, and the receiver is placed 705 mm behind the nominal focal plane to refocus the optics. Obviously, this full PO analysis is impractical for the iterative fitting process in the holographic analysis, where each simulation is ideally required to complete within one second. Nonetheless, we use the simulated results as the gold standard to assess the accuracy of the faster methods developed in the remainder of this section.

There are two very fast methods for beam simulations, but both involve significant approximations. One approach is to employ ray-tracing techniques to find the field in the aperture. Subsequently, a Fourier transform is applied to the aperture field to derive the far-field beam pattern or to get the near-field beam pattern by adding phase correction terms to the aperture field. Although the method is computationally efficient, it neglects diffraction effects in wave propagation from M2 to M1. Especially in our case, where we need to capture the diffraction field

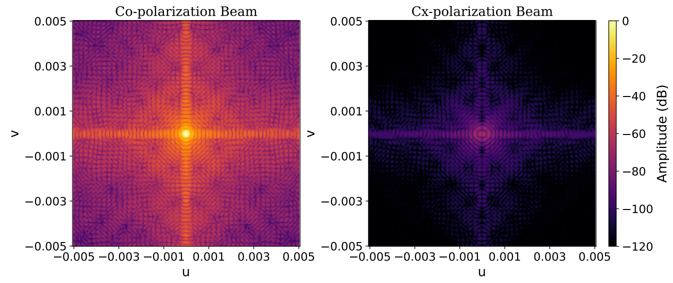

Fig. 3. PO simulations for co- and cross-polarization beam maps of the FYST telescope at 300 GHz, obtained using TICRA GRASP. Both beam maps are normalized to peak of the co-polarization beam. The simulation models a focused beam from a source located 300 m from the telescope. The receiver is positioned 705 mm behind the nominal focal plane to refocus the optical system. The maps cover an angular range of 0.57×0.57 deg^2. The peak cross-polarization level is more than 65 dB below that of the co-polarization beam. Axes are shown in the (u, v) beam coordinates, with $u = \sin\theta_{sky}\cos\phi_{sky}$ and $v = \sin\theta_{sky}\sin\phi_{sky}$, where $(\theta_{sky}, \phi_{sky})$ are the polar angles of the field direction in coordinate system C_{sky} (see Fig. A.1).

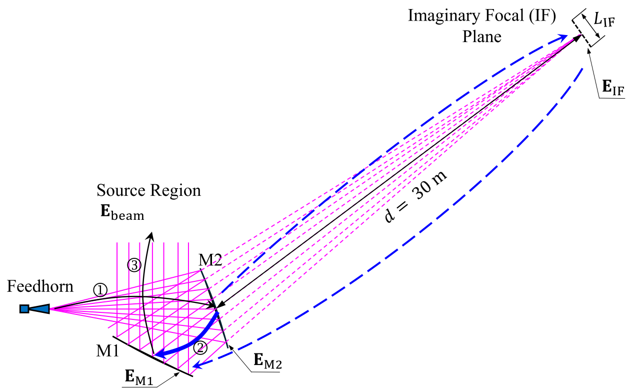

Fig. 4. Beam calculation process of the two-step PO method. The most computationally expensive step 2, field propagation from M2 to M1, indicated by blue solid arrow, is divided into two sub-steps (blue dashed-line arrow) using the imaginary focal (IF) plane. First, the field in the IF plane is computed from the field on M2, where it is confined to a limited region around the focus; then it is propagated to M1, which scatters the field into the sky, producing the final beam map. The fields on M2, in the IF plane, and on M1 are denoted by E_{M2}, E_{IF}, and E_{M1}, respectively. The field calculated in the source region, located 300 m from the telescope, corresponds to the telescope near-field beam map and is denoted by $\mathrm{E}_{\mathrm{Beam}}$. The same flow is used for the scalar diffraction method, with the fields represented by scalar quantities (V_{M2}, V_{IF}, V_{M1}, and V_{Beam}).

on M1 produced by the M2 panel defects and ultimately their impact on the beam map, the ray-tracing technique proves inadequate. Such surface errors introduce diffraction features on M1 that cannot be accurately modeled using ray tracing.

Another approach is based on the angular-spectrum propagation method (Goodman 2005), which deals with the wave propagation from M2 to M1 by decomposing the electromagnetic field on M2 into a set of plane wave components with complex amplitudes using fast Fourier Transform (FFT) techniques, and, after a short distance propagation of these plane wave components, recombining them to obtain the field on a plane close to M1. After applying the phase correction introduced by the curved M1 surface, as computed using ray tracing, the resulting field is further propagated toward the far field. The approach is also efficient due to its FFT-based implementation, but treating the off-axis reflector as a phase converter limits its accuracy primarily to the main beam. The accuracy of these two methods is insufficient for applications that require surface measurement precision better than 3 µm.

We return to the accurate PO analysis to explore ways to accelerate the calculations. A two-step PO analysis method has been developed, which divides the most time-consuming step into two lower-cost PO integrations by introducing an imaginary plane. In addition, the vector PO analysis is replaced by a simple scalar diffraction method to further accelerate the calculation. As our goal is to reduce the computation time to less than a second, additional linear approximations, along with GPU acceleration techniques and a process of saving and reusing intermediate results were employed to further simplify and speed up the process. Throughout this paper, we use the time-harmonic convention $e^{-i\omega t}$ for all electromagnetic fields.

2.1. Two-step PO analysis using imaginary focal plane

The most time-consuming step in the FYST PO analysis is integrating the PO currents on M2 to determine the field on M1. This complexity arises from the similar sizes of the reflectors and their close proximity. At a given point on M1, the phase of the field radiated by the induced current elements on M2 varies rapidly. Therefore, a sufficiently fine sampling of M2 is required to ensure that the phase variation between adjacent samples does not exceed 180°. This difficulty can be overcome by introducing an auxiliary plane and dividing the integration into two fast PO integrations.

The hyperbolic M2 in the classical CD optics has two focal points, as shown in Fig. 4: one coincides with the nominal telescope focal point, i.e., the location of the holographic receiver, and the other is an imaginary focal point located 30 meters behind M2. If the auxiliary plane is placed in the imaginary focus (IF), the scattered field on the plane produced by the currents on M2 is easy to compute. This is because the fields radiated by the M2 current elements have almost the same phase when the optics are focused or nearly focused. This means the PO integration terms vary slowly across the M2 surface and only a small number of sampling points are required for the integration. Subsequently, the scattered field on the IF plane is converted into a set of equivalent surface currents to determine the field on M1. Since most of the power in the IF-plane field is confined to a small spatial region, it is sufficient to sample the field within a limited area to ensure convergence of the field calculation on M1. As a result, the second PO integration is also highly efficient. The blue dashed arrows in Fig. 4 illustrate the flow of the two-step PO analysis.

The equivalent PO currents on the IF plane can be calculated using the field equivalence principle (see Collin & Zucker 1969, Chap. 3). The aim of this principle is to replace the known tangential fields on the IF plane with equivalent electric and magnetic surface currents such that the required tangential boundary conditions are satisfied and the same field solution is reproduced in the region of interest, i.e., in the region between the IF plane and the reflectors. Assuming a null field behind the plane, the fields on the plane are expressed by equivalent electric surface currents, $\mathbf{J} = \hat{n} \times \mathbf{H}$, and magnetic currents, $\mathbf{M} = -\hat{n} \times \mathbf{E}$, where $\mathbf{E}$ and $\mathbf{H}$ represent the electric and magnetic fields on the plane and $\hat{n}$ is the unit normal vector of the plane (taken here to point from the IF plane to M2). The field can also be represented by using only electric currents, $\mathbf{J} = 2\hat{n} \times \mathbf{H}$, or magnetic currents,

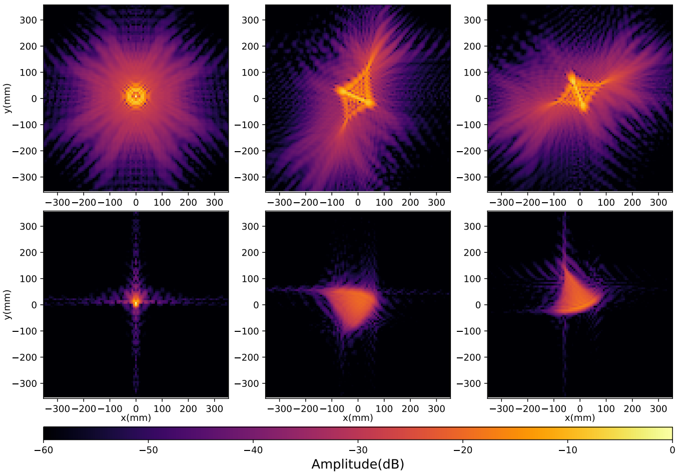

Fig. 5. Virtual diffraction field on the imaginary focal plane for the coma-corrected optics (*top*) and the classical CD optics (*bottom*). *Left to right*: plots correspond to the cases where the receiver is positioned at [0,0], [400 mm, 400 mm], and [400 mm, −400 mm] in the focal plane.

$\mathbf{M} = -2\hat{n} \times \mathbf{E}$, assuming a perfect magnetic conductor or a perfectly conducting surface on the plane. The paper by Bondo & Sorensen (2005) explains the differences in using the three sets of current expressions.

It should be noted that the IF plane lies in the geometrical shadow of the reflector, where no physical scattered field exists. To correctly simulate this virtual field, we numerically back-propagate the field from M2 to the IF plane by reversing the phase factor in the PO integral, using e^{-ikR} instead of the outgoing factor e^{ikR}. Here, $k = 2\pi/\lambda$ is the wavenumber and R denotes the distance from the PO current element to the field point.

In the calculation flow described above, a uniform sampling is applied to all surfaces. The required numbers of sampling points on the reflectors and the IF plane is initially estimated based on the sampling criteria derived from the Fourier-transform case. This is because the calculation flow we perform, from M2 to the IF plane and from IF to M1, etc., can be approximated as Fourier transforms under the assumption of an on-axis paraxial system. We first need to choose the size of the IF plane, which has to be large enough to capture all the relevant information from M2. Simulations indicate that a field map with a size of 500 mm × 500 mm contains 99.9 % of the total power in the plane. Figure 5 (top) shows the simulated IF field, obtained by densely sampling M2 for both the on-axis case and two off-axis cases, where the receiver is positioned almost 600 mm laterally away from the optical axis. The surface shapes of the FYST reflectors have been modified, deviating from classical paraboloid and hyperboloid surfaces to correct for coma errors. As a result, there is no ideal focus behind M1 no longer. This explains why the field in the imaginary plane is more spread out compared to the classical CD optics, as shown in Fig. 5 (bottom).

We start by selecting a square area with side length L_{IF} = 500 mm as the field sampling region in the IF plane. To prevent aliasing errors, the sampling interval on M2, denoted by Δ_{M2}, must be smaller than 48 mm, as derived from the formula

$$\Delta_{\mathrm{M2}} = f \cdot \frac{\lambda d}{L_{\mathrm{IF}}}, \tag{2}$$

where λ is the wavelength, d is the distance from the IF plane to the M2 center, and f is a Nyquist factor less than or equal to 1.

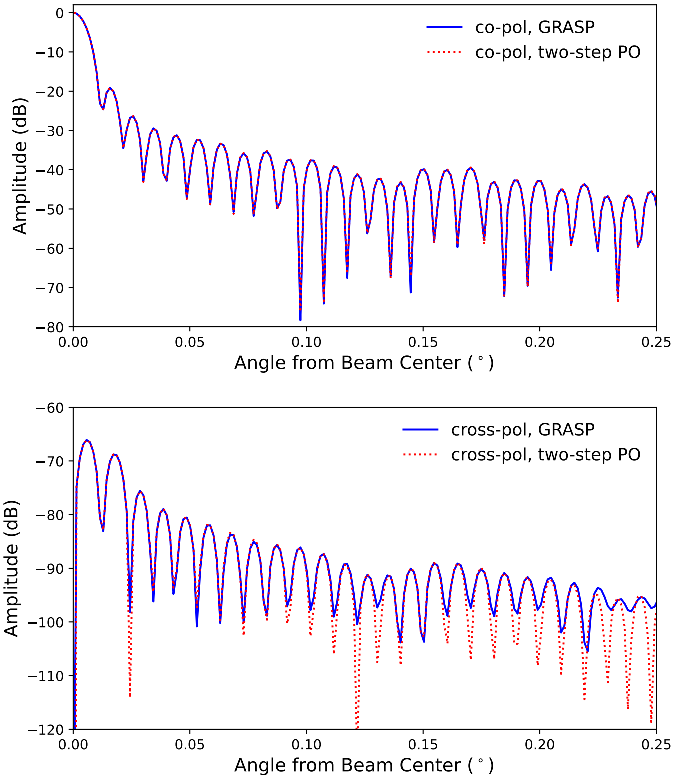

Fig. 6. Cut plots of the simulated co-polarization (*top*) and cross-polarization (*bottom*) beam patterns of the FYST telescope at 300 GHz for the focused optical configuration, obtained using the full PO analysis with the TICRA GRASP and the two-step PO method. The cuts are taken at $\phi_{sky} = 0°$ in the C_{sky} coordinate system defined in Fig. A.1.

By setting f as 0.7, only 15 by 15 sampling points are required on each panel. The sampling points on M1 also need to be fine enough to capture all information coming from IF. By carrying out a series of simulations, we found 12 by 12 sampling points on each panel of M1 are sufficient to obtain converged results.

Figure 6 compares the results of the GRASP PO analysis with those of the two-step PO analysis for the focused optical configuration, demonstrating that the two-step PO can achieve the same level of accuracy as the GRASP analysis, while reducing the runtime to ∼160 s per beam-map simulation using 16 CPU threads on an Intel Core i7-10700.

2.2. Two-step scalar diffraction method

As shown in Fig. 3, the CD telescope exhibits extremely low cross-polarization levels, remaining below −65 dB relative to the peak of the co-polarization beam. In light of this (and considering that the holography measurements do not require cross-polarization beam information), we therefore adopted a scalar diffraction approach based on Kirchhoff's diffraction theory (Born et al. 1999, Chap. 8) in place of the full vector PO analysis to model the field propagation and further simplify the computations. Specifically, we applied the Fresnel-Kirchhoff diffraction formulation to the case of a reflecting surface, as illustrated in Fig. 7. In this configuration, a point source located at P_0 illuminates a reflector surface S, producing an incident scalar field on the surface. The incident field at each surface point $q \in S$ is given by $V_S^q = A\, e^{ikr_0}/r_0$. Within the Fresnel-Kirchhoff description of a reflecting surface, the reflected field just outside the surface, which differs from the incident field by a phase

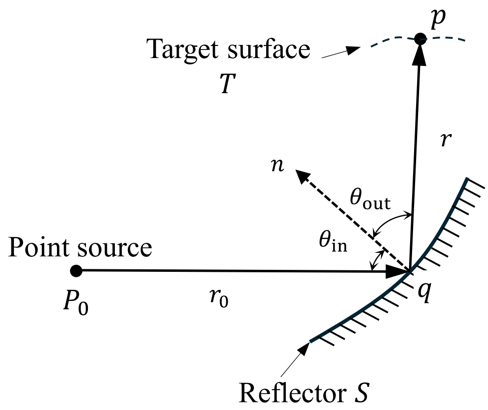

Fig. 7. Illustration of the Fresnel-Kirchhoff diffraction formulation (Eq. (3)) for a reflecting surface. A point source at P_0 illuminates the reflector surface S, producing an incident scalar field. The field reflected from each surface point q on the reflector surface S is treated as a secondary source, and the scattered field at point p on the target surface T is obtained by integrating over S. Here r_0 and r are the distance from P_0 to the point q and from q to p, respectively. The angles $\theta_{\rm in}$ and $\theta_{\rm out}$ denote the local incident and scattering angles at q.

factor of π, $-V_S^q$, acts as the effective source. The resulting scattered field at the observation point p, denoted by V_T^p, can then be expressed as

$$\begin{aligned} V_T^p &= \frac{-i}{2\lambda}\iint_S \frac{-A\ e^{ik(r_0+r)}}{r_0\, r}\left(\cos\theta_{\rm in}+\cos\theta_{\rm out}\right)\,{\rm d}S \\ &= \frac{i}{2\lambda}\iint_S \frac{V_S^q\, e^{ikr}}{r}\left(\cos\theta_{\rm in}+\cos\theta_{\rm out}\right)\,{\rm d}S. \end{aligned} \tag{3}$$

Following the computational flow shown in Fig. 4, we can implement the scalar diffraction method using the same sampling range on the IF plane and the same sampling points on M1 and M2 as those adopted in the two-step PO simulations. In this way, the overall numerical setup is kept identical, and only the propagation formulation is modified. The scalar approach still provides high accuracy in computing the co-polarization beam maps. Compared with the beam simulated by GRASP, the discrepancy remains more than 70 dB below the peak of the co-polarization beam. Figure 8 compares the focused and out-of-focus co-polarization beams computed with the two-step scalar diffraction method and with the GRASP PO analysis. The out-of-focus beam is obtained by offsetting the receiver from the nominal focal plane, which broadens the main beam and reduces the peak gain by ~20 dB. The two-step scalar diffraction approach reduces the computation time to 20 s per beam calculation using 16 CPU threads.

2.3. Approximations to increase the computation efficiency

The holographic fitting process typically requires thousands of iterations to find an optimum solution. To achieve an efficient fitting, we sought to reduce the beam computation time to less than one second per evaluation, so further acceleration of the beam calculation was required. In the fitting process, the forward model is designed to compute beam maps based on given surface deviations, rather than the full reflector geometry. If the surface deviations are small compared with the operating wavelength (e.g., the reflectors of FYST are pre-aligned to within 20 µm), their impact on the beam pattern can be approximated as perturbations to the ideal system. It is assumed that the field

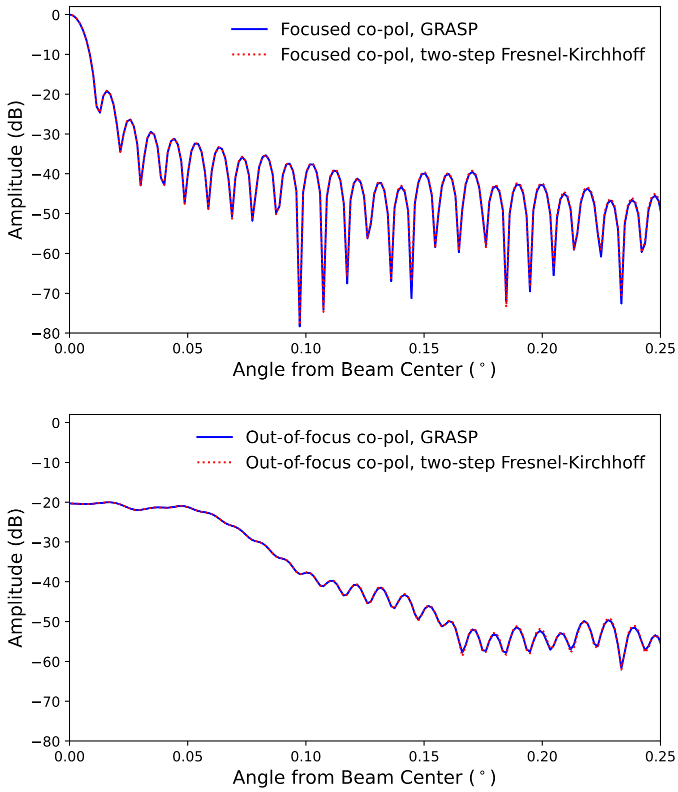

Fig. 8. Comparison of cut plots of the co-polarization beams of the FYST telescope at 300 GHz, obtained using the PO analysis in TICRA GRASP and the two-step scalar diffraction method. The cuts are taken at $\phi_{sky} = 0°$ *Top*: focused beam. *Bottom*: out-of-focus beam.

amplitude on the reflector surfaces remains unchanged, while the phase variation is approximately proportional to the local surface deviation.

The diffraction calculation given by Eq. (3) can then be discretized and written as a matrix-form wave propagation operation, in which a propagation kernel matrix acts on the sampled complex field on the reflector surface. This propagation kernel is independent of the reflector surface deviations, it can be precomputed and stored, and then reused in subsequent fitting iterations. For each beam-map calculation, the given surface deviations are therefore converted into phase corrections to the complex field on the reflector surface, after which the precomputed propagation kernel is applied to obtain the diffraction pattern on the target plane. This avoids recalculating the propagation kernel for each surface-error realization and significantly improves the computational efficiency. The detailed derivation and implementation are given in Appendix C.

Implementing this approach, the required computation time can be reduced to 0.3 s using 16 CPU threads, and to 0.02 s using an NVIDIA GeForce RTX 3070 GPU. The computation times for the GRASP PO analysis, two-step PO method, two-step Fresnel-Kirchhoff method, and the approximation approach are summarized in Table 1.

2.4. Diffraction effect of the reflector panel edges

Although PO analysis and the acceleration methods described above provide accurate and efficient simulations for large reflectors, they do not account for the effect of surface discontinuities caused by panel gaps. The FYST reflectors are made of 146 panels, with a 1.2 mm gap between each panel to accommodate

Table 1. Computation times for the four approaches.

Method	Time
GRASP PO	10 days (including convergence test)
Two-step PO	160 s
Two-step Fresnel-Kirchhoff	20 s
Approximate model (CPU)	0.3 s
Approximate model (GPU)	0.02 s

Notes. GRASP PO was run on two Intel Xeon E5-2697 v4 processors (2.65 TFLOPS, FP32). Methods 2–4 were run on an Intel Core i7-10700 processor (1.28 TFLOPS, FP32). GPU calculations were performed on an NVIDIA GeForce RTX 3070 (20.1 TFLOPS, FP32). FP32 denotes single-precision 32-bit floating-point arithmetic, and TFLOPS denotes 10^{12} floating-point operations per second. These values indicate only the theoretical peak performance.

thermal expansion. These discontinuities cause the induced surface currents near the panel edges to differ from the PO currents. The difference is concentrated in the panel boundary region, only at a distance on the order of a wavelength. Compared with the size of the FYST panels, about $700 \times 700\,\mathrm{mm}^2$, we think the edge diffraction effect can be neglected. However, the presence of 146 panels with 584 edges necessitates an assessment of the cumulative effect.

The physical theory of diffraction (PTD; Ufimtsev 2014; Paknys 2016) is the standard technique used to account for panel edge diffraction. We carried out the PO-plus-PTD analysis and PO-only analysis at 100 GHz, 150 GHz and 300 GHz using the GRASP package. Their differences, which are normalized to the value of the beam peak and shown in Fig. 9, give the impact of the panel edges on the telescope's diffraction beam. It can be seen that the panel edges produce a pattern of sidelobes in the crossover region of the beam map. The maximum of the difference is −60.5 dB relative to the beam peak at 100 GHz and −64 dB at 150 GHz. At 300 GHz, the edge effects in the beam maps remain below −70 dB relative to the beam peak, which can be neglected in the holography measurement.

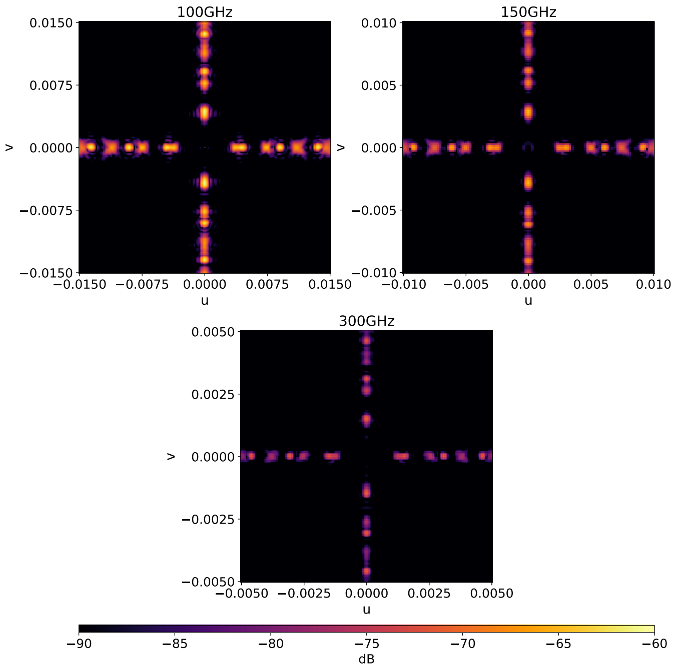

Fig. 9. Sidelobe pattern produced by the panel edges of the FYST reflectors for the focused optics at 100 GHz (*top-left*), 150 GHz (*top-right*), and 300 GHz (*bottom*). These patterns are calculated by taking the difference between PO-only simulation and PO-plus-PTD simulation, normalized by the value at the map center. To ensure consistency and enable meaningful comparisons, the map size is scaled inversely with frequency.

3. Implementation of fitting process

3.1. Parameterize surface deviations of reflectors

To implement the numerical fitting process and convert the measured beam maps into surface error maps of the two reflectors, the surface deviations must be parameterized. In the case of the FYST holography, the surface deviations are parameterized on a panel-by-panel basis. The panels on M1 and M2 are nearly square in shape, and each panel has five adjusters along the z-axis, one at the center of the panel and the remaining four at the corners of a rectangle (see Fig. D.1). We choose these adjuster displacements as the parameters to describe the surface deviations and fit them to the measured data. With the five z-axis adjusters, we can control five surface error terms for each panel: piston, x- and y-tilt, symmetrical curvature, and twist distortions. Figure D.1 illustrates the corresponding panel distortion modes induced by the adjuster displacements. These error terms can be represented by a second-order polynomial, as defined in Eq. (4), where x and y in the equation are the coordinates of a point on the panel surface.

$$\epsilon_{panel} = a_0 + a_1\,x + a_2\,y + a_3\,xy + a_4\left(x^2 + y^2\right). \tag{4}$$

Substituting the adjuster displacements and their coordinates (x, y) on the panel into the equation, we can find the linear relationship between the polynomial coefficients a_{0-4} and the adjuster displacements, as expressed in Eq. (D.5). Therefore, for a given set of adjuster displacements on M2 and M1, the corresponding reflector surface errors can be determined panel by panel.

In this representation, the reflector surface errors are written as $\epsilon_{\mathrm{M2}}(\boldsymbol{\delta}_{\mathrm{M2}})$ and $\epsilon_{\mathrm{M1}}(\boldsymbol{\delta}_{\mathrm{M1}})$, with $\boldsymbol{\delta}_{\mathrm{M2}}$ and $\boldsymbol{\delta}_{\mathrm{M1}}$ denoting the corresponding adjuster-displacement vectors on M2 and M1 respectively. M2 comprises 69 panels (345 adjusters), while M1 consists of 77 panels (385 adjusters). Hereafter, $\boldsymbol{\delta}_{\mathrm{M2}}$ and $\boldsymbol{\delta}_{\mathrm{M1}}$ are referred to as the surface parameters to be fitted for the reflector-surface reconstruction.

Alternatively, if the detailed panel distortions are not of concern and the focus is on large-scale surface deformations, we can use a set of orthogonal basis functions to describe the surface deviations of the entire reflector, such as Zernike polynomials for circular or elliptical reflector apertures or their rectangular derivatives (Born et al. 1999; Niu & Tian 2022). This is particularly useful for diagnosing some issues, such as thermal distortions on reflectors and back-up structures, and gravity-induced deformations. The maximum order of the polynomials is determined by the surface spatial resolution required for setting the reflectors. Zernike circular polynomials have been adopted in the OOF holography technique to analyze large- and medium-scale reflector deformations at different elevation angles for telescopes such as the Green Bank Telescope (Nikolic et al. 2007b) and Effelsberg 100-m telescope (Cassanelli et al. 2024).

3.2. Parameterization of systematic effects

In practical holography measurements, there are several factors, aside from the surface errors in the reflectors, that can lead to a mismatch between the observed data and simulations. These include an error in the position of the receiver mounted at the focal plane, an offset in the pointing of the telescope, and uncertainty of the assumed distance from the telescope to the source. While these errors are small, they create either a slope or a curvature in the phase at the telescope's aperture plane. To reduce their impacts on surface measurement accuracy, we must account for these effects in the beam simulation model. These can be represented by a phase correction factor, $\Delta\phi_{ap}(x, y)$, applied to the telescope aperture field in the beam calculations. The phase factor $\Delta\phi_{ap}(x, y)$ is expressed as

$$\Delta\phi_{ap}\,(x, y) = \beta_0 + \beta_1\, x + \beta_2\, y + \beta_3\, \left(x^2 + y^2\right), \tag{5}$$

where x and y here are the coordinates of the field point in the aperture plane. The coefficients β_0 accounts for the reference phase offset, β_1 and β_2 for the phase slope in $x-$ and y-directions, and β_3 for the optical defocus caused, for example, by a receiver axial offset.

In addition, the amplitude distribution of the field across the aperture may not exactly match the assumed model, due to uncertainties in the width of the receiver beam pattern (e.g., a two-dimensional Gaussian beam) and in the source illumination pattern over the telescope's aperture. For small deviations in the Gaussian beam width and beam-center position, the resulting mismatch can be approximately parameterized by an amplitude-only multiplicative correction applied to the aperture field. This correction factor is motivated by the first-order perturbation of a two-dimensional Gaussian beam with respect to small beam-center offsets and beam-width variations. Rather than explicitly expanding the Gaussian parameters, the resulting mismatch is represented by a low-order polynomial in the transverse coordinates. The amplitude correction is written as

$$A_{ap}\,(x, y) = 1 + \Delta A_{ap}\,(x, y)\,, \tag{6}$$

where

$$\Delta A_{ap} = \alpha_0\; +\; \alpha_1\, x + \alpha_2\, y + \alpha_3\, xy + \alpha_4\, x^2 + \alpha_5\, y^2. \tag{7}$$

Here, the linear terms mainly capture beam-center offsets, while the quadratic terms describe low-order beam-width and ellipticity mismatches. The cross term xy allows for coupling between the two transverse directions, which can arise from beam rotation or other small deviations from the nominal Gaussian model. The amplitude and phase correction factors are combined into a single multiplicative correction factor applied to the aperture field to compensate these systematic effects. Then the aperture correction factor denoted by $C_{ap}(x, y)$ is expressed as

$$C_{ap}\,(x, y) = \left(1 + \Delta A_{ap}\,(x, y)\right)\, e^{i\Delta\phi_{ap}(x,y)}. \tag{8}$$

After discretization, the factor $C_{\rm ap}(x, y)$, parameterized by $\boldsymbol{\alpha} = (\alpha_0 \ldots \alpha_5)$ and $\boldsymbol{\beta} = (\beta_0 \ldots \beta_3)$, is written as a vector $\mathbf{C}_{\rm ap}(\boldsymbol{\alpha}, \boldsymbol{\beta})$ and incorporated directly into the sampled field on M1 through an element-wise multiplication. Accordingly, in the beam simulation procedure defined by Eq. (C.8) defines the beam prediction function, Eq. (C.8c) is replaced by

$$\mathbf{V}_{\rm Beam} = \mathbf{K}_{\rm M1\to Beam}\left(\mathbf{V}_{\rm M1} \odot \mathbf{C}_{\rm M1}\,(\epsilon_{M1}) \odot \mathbf{C}_{\rm ap}\,(\boldsymbol{\alpha}, \boldsymbol{\beta})\right). \tag{9}$$

For convenience, the full beam calculation described by Eqs. (C.8a) and (C.8b) and Eq. (9) is denoted by the beam prediction function, F, such that

$$\mathbf{V}_{\rm Beam} = F\,(\boldsymbol{\delta}_{\rm M2}, \boldsymbol{\delta}_{\rm M1}, \boldsymbol{\alpha}, \boldsymbol{\beta})\,. \tag{10}$$

The coefficients $\boldsymbol{\alpha}$ and $\boldsymbol{\beta}$ are hereafter referred to as the systematic parameters, and will be fitted together with surface parameters in the following analysis. It should be noted that each beam calculation is assigned an independent set of $\boldsymbol{\alpha}$ and $\boldsymbol{\beta}$, whereas the surface parameters are shared among all beam maps. Since the FYST holography analysis requires five independent beam maps, five independent sets of systematic parameters are introduced.

3.3. Fitting procedure

The measured complex beam maps are preprocessed to remove systematic fluctuations, smoothed to improve the S/N, and resampled onto a coarser grid (with spacing smaller than the antenna beam size). The processed measurements are then collected into a data vector $\boldsymbol{D} = (D_1, D_2, \ldots, D_N)$, where D_j denotes the processed complex field at the jth sampling point. The vector $\boldsymbol{D}$ is used as the input to the analysis.

In the fitting procedure, the measured data, $\boldsymbol{D}$, are first normalized to have unit total power and zero phase at the map center. Then for a given set of surface and systematic parameters, the beam maps are computed using the beam prediction function Eq. (10). The computed beam maps are assembled into a vector, $\boldsymbol{Y} = (Y_1, Y_2, \ldots, Y_N)$, with the same size as $\boldsymbol{D}$. The same normalization procedure is applied to $\boldsymbol{Y}$ to ensure consistency with the measured data. Initially, we assume the reflectors to be perfect, and the measurement system to be fully consistent with the design. The mismatch between the calculated data and observed data is quantified by the vector difference $E_j = Y_j - D_j$. Implementing a fitting process to minimize the mismatch, for example, minimizing the sum of $|E_j|^2$ over all the field points, we can find the parameter values that best reproduce the measured beams. The values of the fitted surface parameters are used to reconstruct the reflector surface deviations. The fitted systematic errors are expected to be a slight deviation from the design assuming the holographic system has been carefully precalibrated and measured.

It should be noted that degeneracies exist between the systematic parameters and the surface parameters. For example, a defocus error expressed by the second-order phase term in Eq. (5) can also be produced by the curvature surface errors on M1 or M2. To ensure that linear and defocus-like components are not absorbed into the surface parameters, a regularization term is added to the quantity $(\sum_j |E_j|^2)$ to be minimized, which constrains the surface deviation to remain small. The new quantity to be minimized is given by the following equation,

$$Residual = \sum_j |Y_j - D_j|^2 + \Gamma\left[\sum_n \left(\delta^n_{M2}\right)^2 + \sum_m \left(\delta^m_{M1}\right)^2\right], \tag{11}$$

where Γ acts as a weighting factor to control the influence of the regularization term in the fitting process. The value of Γ

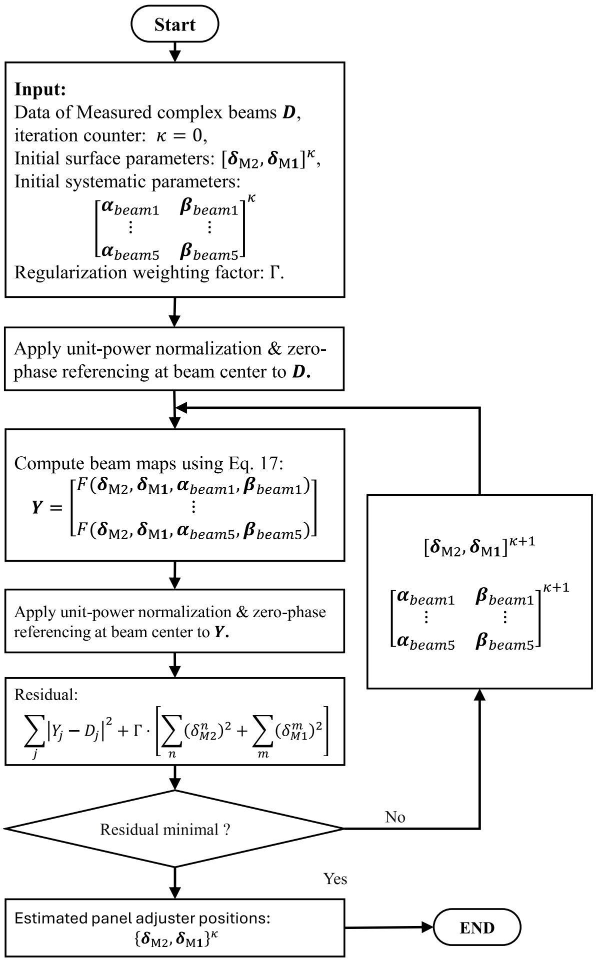

Fig. 10. Flowchart of the fitting procedure used to determine the reflector adjuster displacements, $\boldsymbol{\delta}_{\mathbf{M2}}$ and $\boldsymbol{\delta}_{\mathbf{M1}}$, from five beam calculations. The fitted displacements are then used to reconstruct the reflector surface errors and correct the panel distortions. $\boldsymbol{\alpha}_{\text{beam1-beam5}}$ and $\boldsymbol{\beta}_{\text{beam1-beam5}}$ denote the systematic parameters assigned separately to the five beam maps.

is predefined by the user before the fitting analysis, determined through simulations by examining its effect on the reconstructed surface accuracy across several orders of magnitude, and then held fixed during the fitting. We also found that initially fitting only systematic parameters and then using the results as inputs to the full parameter fitting can significantly improve the overall efficiency and accuracy of the fitting process. The fitting procedure is summarized in Fig. 10 as a flowchart. The Broyden–Fletcher–Goldfarb–Shanno (BFGS) algorithm (Nocedal & Wright 2006), which is a gradient-based optimization method, is used to determine the optimal surface parameters. The algorithm can approximate the gradient ($\nabla Residual$) numerically using finite differences; however, with on the order of 1000 variables, this becomes computationally intensive, as the computational cost scales with both the number of variables and the time required for each forward function evaluation. To address this, we adopt the automatic differentiation technique (Nocedal & Wright 2006), which decomposes the complex function into a sequence of basic operations and computes the derivatives of the function by applying the chain rule to these simple operations. This approach makes the computational cost largely independent of the number of variables while providing fast and accurate gradient evaluations. We implement this technique using the PyTorch package (Paszke et al. 2019).

4. Simulations

The feasibility, accuracy, and optimal setup of the technique have been investigated through a series of simulations of the beam measurement and fitting process for the FYST holographic system. In the system, the source is 300 m from the telescope rotational axis, which shifts the best focus to about 705 mm behind the astronomical focal point. Since this technique does not require the receiver to be located at the best focus, the receiver is intentionally moved forward by 105 mm from the new focus to spread out the beam as shown in Fig. 8. The purpose of this defocus is to reduce the required dynamic range for the beam measurement system by ~20 dB.

A set of random displacements with an rms magnitude of 30 µm shown in the top panel of Fig. 13, is introduced to the panel adjusters. The beam maps distorted by the panel deformations, denoted by $\tilde{\boldsymbol{D}}$, are theoretically calculated using the PO method with the receiver placed at five points in the focal plane, one at the center and four at the corners of a square. The optimal separation distance of the four corner points has been studied by simulations. The computed beam maps, $\tilde{\boldsymbol{D}}$, after adding random measurement noise and systematic errors, are then used as the measured data $\boldsymbol{D}$, which can be expressed by the following equation:

$$D_j = \tilde{D}_j \cdot \left(1 + \Delta G_j\right) e^{i\,\Delta\phi_j} + n_j, \tag{12}$$

where n_j is a set of random Gaussian variables with zero mean and an RMS of s_n, representing additive noise, and ΔG_i and $\Delta\phi_i$ are multiplicative errors which could arise from gain and phase fluctuations of the instruments or variations of the atmosphere between the telescope and the source.

We use the panel adjuster displacements as the surface parameters to be fitted. In total, 780 parameters are included in the fitting process: 730 surface parameters and 50 for systematic effects. Fitting the panel adjuster movements cannot precisely separate large-scale surface errors, as these remain nearly degenerate between the two reflectors. However, by iteratively performing holographic measurements and adjusting the panels, such errors can still be effectively minimized. The residual large-scale errors on the two reflectors tend to compensate for each other and thus have a negligible impact on the telescope's scientific performance.

4.1. Effect of additive random noise in measured maps

The relationship between the fitted surface accuracy, the S/N of the measurement system, and the receiver separation distance is investigated. We express the S/N in terms of peak S/N, defined as the ratio of the peak amplitude, for the case of perfect reflectors and with the receiver at the 'best' focus, to the rms σ of the noise.

The effect of thermal noise on the surface accuracy is illustrated in Fig. 11, which shows the RMS surface reconstruction error obtained from simulated data with peak-S/Ns ranging from 55 to 70 dB, corresponding to amplitude ratios of approximately 560 to 3200. For each specified peak-S/N, 10 independent noise realizations were simulated. The reconstruction error is defined as the RMS of the difference between the reconstructed and true reflector surfaces. The simulations indicate that a peak-S/N of greater than 70 dB is required to achieve an accuracy better than 1 µm. For the out-of-focus setup, the required measurement S/N

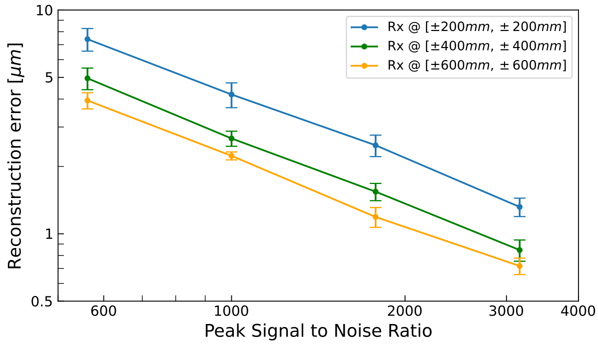

Fig. 11. RMS surface reconstruction error (relative to the true reflector surfaces) as a function of S/N. The three traces correspond to results obtained using different sets of receiver positions, as indicated in the legend. Symbols show the mean over 10 independent noise realizations, and error bars indicate the standard deviation across the realizations.

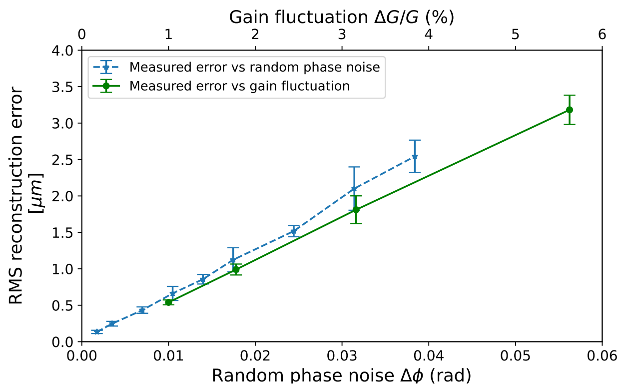

Fig. 12. RMS surface reconstruction error as a function of random phase error and gain variation in the holographic system.

should be larger than 50 dB. Figure 11 also suggests that using a small spacing (±200 mm in each direction) produces rather large errors, while ±400 mm is good and ±600 mm is only slightly better. The following simulations therefore adopt a receiver spacing of ±400 mm.

4.2. Effect of systematic errors

The multiplicative terms in Eq. (12) are used to model systematic errors such as gain fluctuations and phase variations in the measurement system during beam scanning. These effects are random but do not exhibit the characteristics of white noise. To make them more realistic, they are filtered to produce smoother low-frequency variations over time.

In practice, the low-frequency components can be calibrated by frequently pointing the telescope to the center of the beam map and recording the amplitude and phase. Smooth functions of time are then fitted to the amplitude and phase and used to correct the measured data. After this calibration process is applied, the residual gain and phase variations can be modeled by white noise with a small rms value. The simulations indicate that gain variations at the level of 1%, $< \Delta G_i^2 >^{1/2} = 0.01$, and phase variations, $< \Delta\phi^2 >^{1/2} = 0.01$ rad, each degrade the measurement accuracy by about 0.5 μm (Fig. 12).

In addition to instrumental drifts, atmospheric turbulence between the source and the telescope can introduce additional

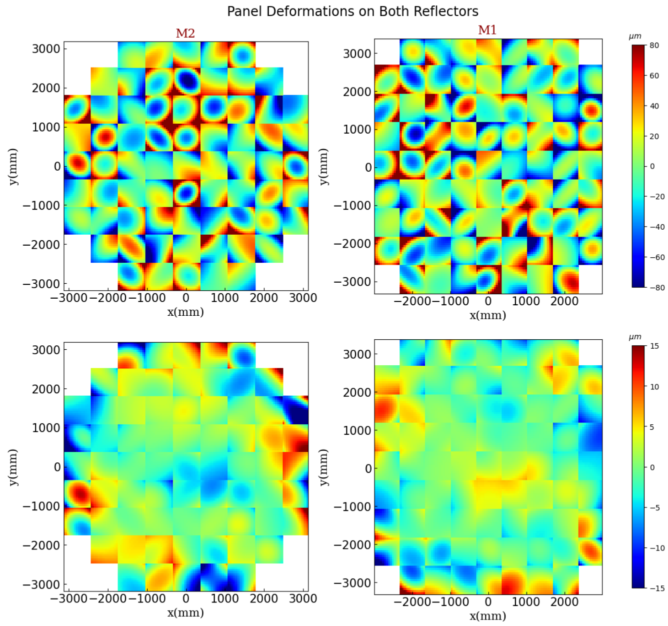

Fig. 13. *Top*: surface deformations of M1 (*right*) and M2 (*left*) with 30 μm RMS random movements of the panel adjusters. *Bottom*: deviation of the best-fitting surfaces from the input surfaces for the measurement beam maps with a peak-S/N of 65 dB, 1% gain fluctuations, 0.5° phase variations, and 2″ peak-to-peak pointing errors.

phase errors through refractive-index variations along the signal's propagation path. At millimeter wavelengths, these fluctuations are driven by spatial and temporal variations in water vapor within turbulent cells. In practical near-field holography, a reference receiver placed close to the telescope aperture provides a common-mode phase reference, so most atmospheric fluctuations can be effectively canceled. However, residual differential path variations may remain, particularly under rapidly varying atmospheric conditions such as strong winds. This implies that atmospheric stability should be characterized prior to beam measurements and that the frequency of the beam-center calibration process should be adjusted accordingly.

We also investigated the impact of pointing errors during beam scanning on the surface-fitting accuracy. A simulation incorporating "random-walk" pointing errors with a peak-to-peak amplitude of 2″ over the entire scan in both azimuth and elevation directions yielded a fitting error of 2.5 μm. This means that the fitting technique is sensitive to the precision of the telescope pointing. Figure 13 shows the deviations of the best-fitting surfaces of the two reflectors for a case with a measurement peak S/N of 65 dB, and systematic errors of 1% gain fluctuation, 0.5° phase variations and 2″ telescope pointing errors. The overall RMS of the measurement surface errors is about 3 μm.

5. Experiments

A small CD telescope with a 400 mm aperture, representing a 1/15th scale model of the FYST reflectors, was constructed to demonstrate the feasibility of the proposed holographic technique. The experimental setup for the small telescope is illustrated in Fig. 14. The laboratory test was conducted at 300 GHz using the same hardware as the FYST holography system, including the receiver and source modules described in Ren et al. (2020). The two reflectors were mounted on an aluminum frame

Fig. 14. Laboratory holographic testbed. *Left*: 1/15th-scale FYST reflector system (400 mm diameter) with the signal receiver (①) mounted at the focal plane; the reference receiver (②) is placed beside the telescope to provide a phase reference. *Right*: 300 GHz transmitter source (③), mounted on an XY translation stage (④), is positioned approximately 5 m from the center of the M1 reflector to illuminate the telescope. The telescope beam is measured by raster-scanning the source using the XY stage.

to position them at the correct tilt angle, with the entire structure securely mounted to the laboratory wall (see Fig. 14 left). The signal generated by the holographic source module propagates from the right hand side of the telescope, reflects off its two reflectors (M1 and M2), and travels upward to a signal receiver located in the focal plane. The receiver is mounted vertically on a metal plate, oriented downward to intercept the signal collected by the reflectors.

Because the reflectors are fixed to the wall, beam maps are measured by scanning the source. As shown in Fig. 14 (right), the source is mounted on an XY stage approximately 5 meters away from the reflectors. The receiver mounting plate includes five positions for beam measurements: one at the center and four at the corners of a 100 mm square. A reference receiver was installed adjacent to the telescope and used to establish a phase reference for complex beam-pattern measurements. A spatial resolution of 10 mm was specified for the reconstructed reflector surface error maps, which requires a beam-map angular extent of approximately 0.1 rad. For a source distance of 5 m, this corresponds to a scanning range of about 500 mm.

5.1. Classical "single-map" holographic analysis

Copper foils with a thickness of 50 μm were applied to both reflector surfaces to introduce artificial piston-type surface errors, which were used to evaluate the feasibility of the proposed holographic technique and system. Figure 15 shows the locations of the error patches on the reflectors. These errors distorted the wavefront of the incoming signal across the aperture. The left panel of Fig. 16 shows the distorted beam measured with the receiver mounted at the center of the focal plane. Using the conventional near-field holography analysis, we derived the aperture-plane phase distribution of the optics. After removing the overall phase slopes and curvature across the aperture, the resulting aperture-phase distributions are shown in the right panel of Fig. 16. It is evident that the phase contributions from the copper patches on M1 and M2 overlap and cannot be discriminated, highlighting the degeneracy problem in the two-reflector optical system.

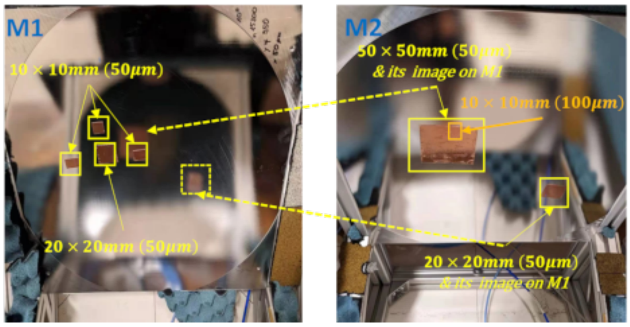

Fig. 15. Artificial surface errors on M1 and M2 introduced using copper tape of thickness 50 μm. The figure illustrates the size and locations of the copper patches applied to the reflector surfaces. The projection of the largest copper patch on M2 overlaps with the error patches on M1.

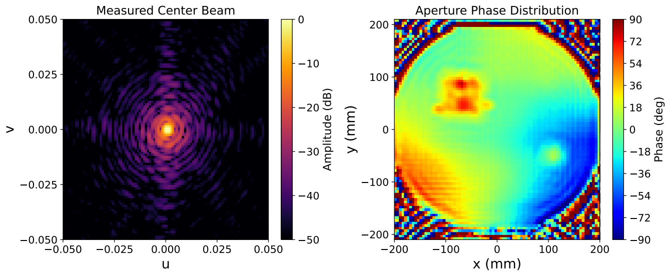

Fig. 16. *Left*: measured beam map with the receiver located at the center of the focal plane, for the reflector surface errors shown in Fig. 15. *Right*: phase distribution on the aperture plane, reconstructed from the measured beam map. The phase errors introduced by the copper patches on M1 and M2 are observed to overlap significantly.

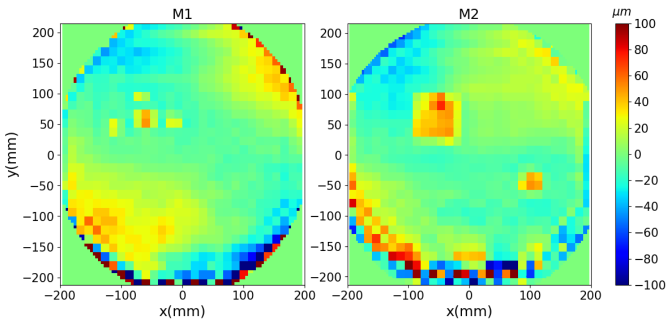

Fig. 17. Best-fit surface-error maps for the two reflectors, M1 (*left*) and M2 (*right*), reconstructed using 30 by 30 rectangular grids. The reconstruction is based on the 300 GHz beam measurements shown in the top panel of Fig. 19.

5.2. Multi-map holographic analysis

Using the multi-map holographic analysis, the other four off-axis beam maps (shown in Fig. 19, top) were measured to fit the surface deviations of the two reflectors. The surface error distributions on M1 and M2 were expressed by 30 × 30 uniform grids, with each cell measuring about 13.3 × 13.3 mm^2. In total, 1800 surface parameters and 50 systematic parameters were fitted. By leveraging GPU acceleration, the fitting process completed within 10 minutes. Figure 19 compares the contours of the measured beam maps with those of the corresponding best-fit beam maps, showing very good overall agreement.

Figure 17 shows the best-fit surface error maps. Comparison with the known copper patch locations in Fig. 15 confirms that all introduced surface errors were successfully identified and correctly attributed to the respective reflectors. The statistical uncertainty of the measurement was assessed by repeating the experiment multiple times, which showed random variations in the reconstructed surface error maps with an rms scatter of less than 1 µm. The stiffness of the 50 µm-thick copper foil caused poor contact and surface roughness, limiting the precision of the introduced errors and preventing reliable accuracy assessment. To improve this, more flexible 10 µm and 20 µm foils were applied. The foil locations and the corresponding best-fit surface error maps are shown in Fig. 18. The cross-sectional plot in Fig. 18, taken along the indicated line, shows a measured copper patch thickness of approximately 11 µm, in close agreement with the nominal height of 10 µm. This result confirms that the new holographic technique achieves a measurement accuracy within 3 µm.

The error maps in Figs.17 and 18 both show relatively large deviations near the reflector edges. This is mainly because the fields in these regions are weakly illuminated due to the receiver illumination pattern, so their impact on the beam is relatively small compared with surface errors in the central regions of the reflectors. As a result, the surface parameters in these edge regions are less well constrained by the beam data and are more sensitive to systematic errors.

5.3. Large-scale errors

In addition to the surface errors introduced by the copper patches, a twist-like deformation was observed on both reflectors, as shown in Fig. 17. To analyze such large-scale surface errors, it is more effective to represent them using a set of Zernike circle polynomials (Born et al. 1999). For this purpose, the elliptical apertures of both reflectors were normalized to a unit circle, and Zernike polynomials up to the seventh radial order were employed. This yields 36 Zernike terms per reflector. We fixed the first three modes (piston, x-tilt, and y-tilt) and the defocus mode to zero and fitted the remaining 32 coefficients for each reflector. Figure 20 shows that the observed twist-like pattern can clearly be identified as arising from a deformation of M1. This finding was independently confirmed by mechanical measurements and corrected before obtaining the measurements shown in Fig. 18. By increasing the radial order of the Zernike polynomials up to the 30th order, some local patches with sizes of about 20 mm become visible in the reconstructed surface-error maps. However, the high-order reconstruction is less robust and should be interpreted with caution. Because the Zernike basis is not strictly orthogonal over the truncated-elliptical reflector rim, high-order modes can become coupled, making the corresponding coefficients more sensitive to noise and modeling uncertainties. A more detailed treatment of high-resolution surface reconstruction using Zernike polynomials, including aperture-specific orthogonalization and regularization, is beyond the scope of the present work and will be addressed in a future study. The high-order result is therefore shown only for qualitative comparison with the low-order reconstruction. In particular, the twist-like deformation pattern remains qualitatively visible and is consistent with the large-scale structure recovered by the low-order fit.

The holographic analysis was also performed for an out-of-focus configuration, in which the receiver was moved 80 mm closer to M2. The best-fitting surface profiles were consistent with those obtained from the in-focus beam measurements. The

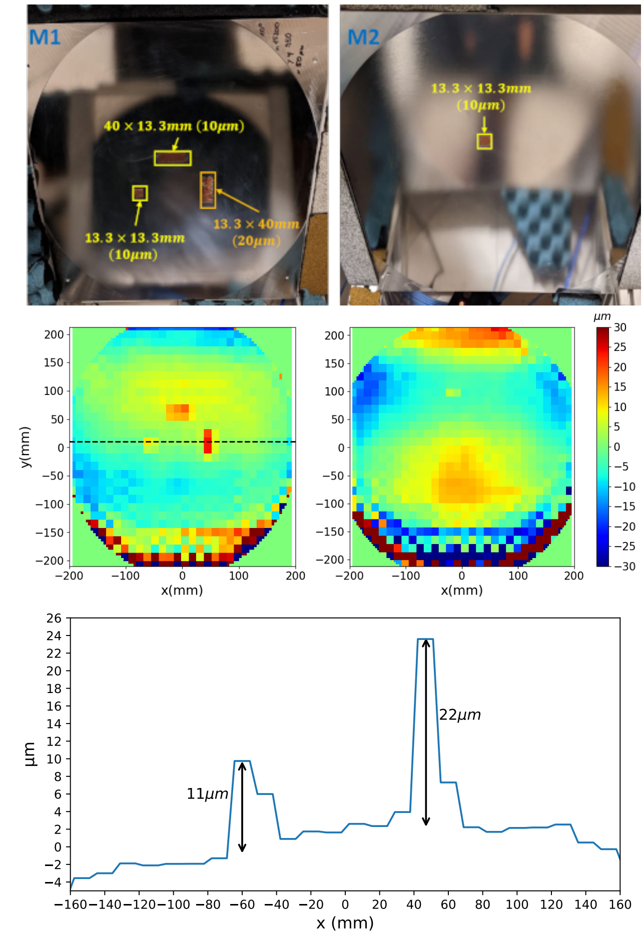

Fig. 18. *Top*: surface errors on M1 and M2 produced by copper foils of thickness 10 µm and 20 µm. Middle: best-fit surface error maps. *Bottom*: cross-sectional plot along the dash line indicated in the middle panel.

broadening of the optical beam by the out-of-focus configuration reduced the required dynamic range by approximately 10 dB.

6. Discussion and conclusions

We present a novel holography technique for measuring the surface errors of large CD reflectors based on measurements of multiple beam maps at different focal-plane positions, parameterization of the surface errors, and application of a numerical fitting approach. The feasibility and accuracy of the new technique have been verified through numerical simulations for FYST and experimental tests on a small CD reflector system.

Compared with conventional single-beam holography and phase-retrieval techniques, the key advantage of the proposed multi-map approach is its ability to disentangle the surface-error contributions from the two reflectors in CD systems. In a CD optical system, the wavefront distortions induced by surface errors on the primary and secondary reflectors are strongly degenerate in a single beam map, so standard holography often recovers an effective combined error rather than two independent surface maps. By measuring beams at multiple well-separated receiver positions in the focal plane, our method, together with the data-fitting procedure developed here, can robustly reconstruct the surface-error contributions on both reflectors. This capability is particularly important for FYST, which is designed

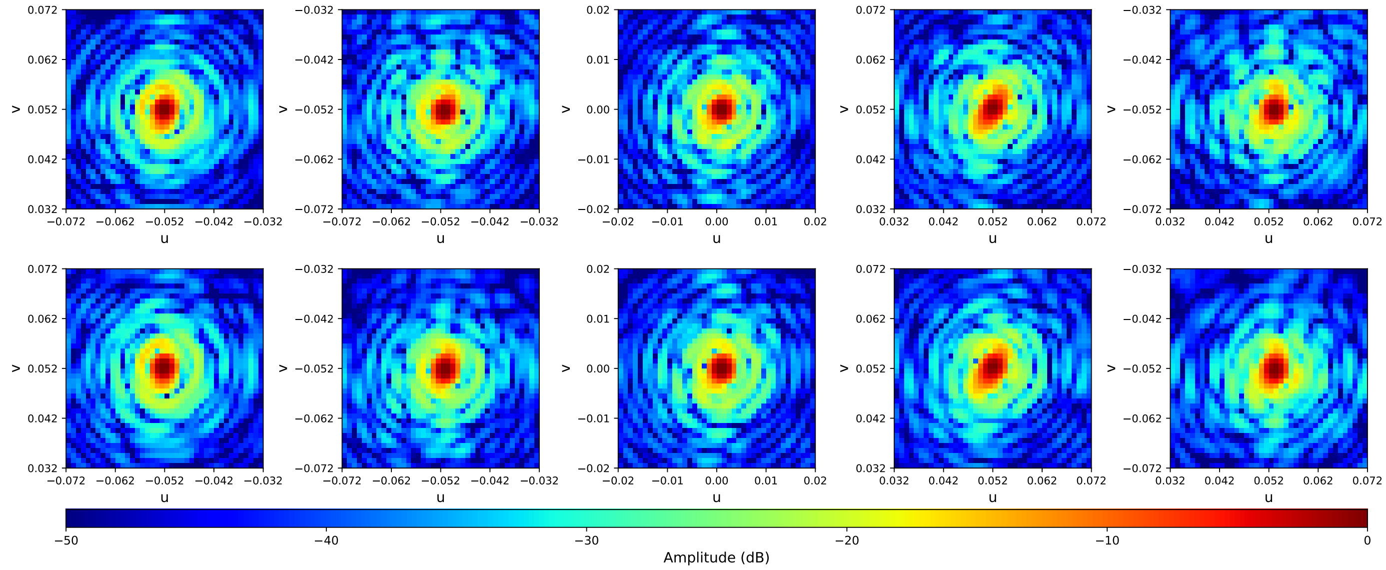

Fig. 19. Comparison between measured and fitted telescope beams at 300 GHz. *Top*: five measured beam maps with the receiver positioned at (50 mm,50 mm), (50 mm,−50 mm), (0 mm,0 mm), (−50 mm,50 mm), and (−50 mm,−50 mm) relative to the focal-plane center (from *left to right*). These offsets correspond to ($\pm 50\lambda, \pm 50\lambda$) at 300 GHz *Bottom*: corresponding best-fitting beam maps obtained from the multi-map holography analysis. The beam-map axes are shown in angular (u, v) coordinates converted from the laboratory source scan positions measured with the XY translation stage. The color scale shows normalized beam power in dB, and each beam map is normalized to its own peak value.

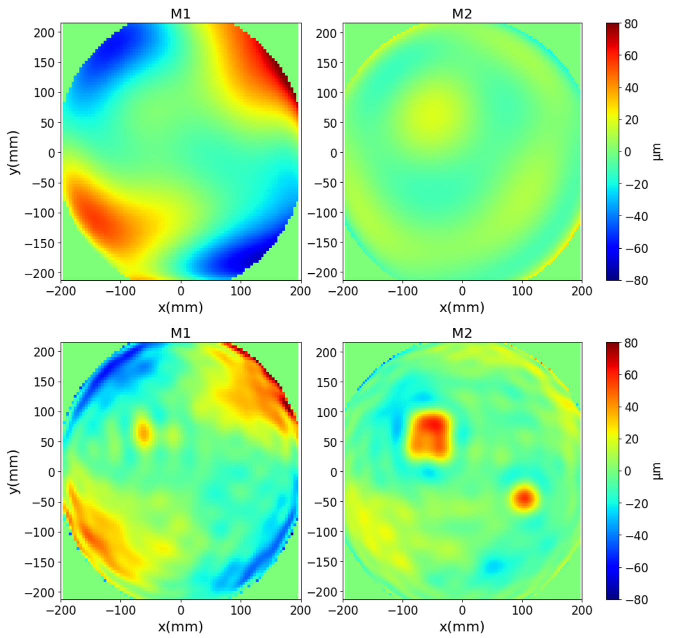

Fig. 20. Surface deviations of the small CD reflectors analyzed by fitting the coefficients of the Zernike polynomials with the maximum orders, i.e., the seventh (*top*) and 30th (*bottom*) orders. The left hand surface map shows the measured twist-like large-spatial errors on M1.

to deliver a large field of view to maximize survey speed and therefore requires accurate correction of surface errors on both reflectors to maintain high optical efficiency across the entire field of view, thereby enabling the sensitivity and mapping speed required for large-area millimeter and submillimeter astronomy (Ramasawmy et al. 2022).

The laboratory measurements further demonstrate that the multi-map technique can discriminate between surface errors on the two reflectors with the intended spatial resolution and measurement accuracy. Although this work is motivated by CD telescopes, the methodology is not specific to CD optics and can be readily extended to other two-reflector systems.

The new data-fitting framework offers important advantages for accounting for systematic errors in the measurement system by explicitly parameterizing them and incorporating them into the beam model. In particular, uncertainties in the receiver position, imperfections in the feed-illumination pattern, and telescope-pointing offsets can be treated as additional fitting parameters. This joint modeling enables separation of true reflector-surface deformations from measurement-system effects and facilitates identification of potential misalignments or inconsistencies that might otherwise go unnoticed. Furthermore, the data-fitting framework developed here is general and can be adapted to the analysis of conventional single-beam holography, providing a more flexible alternative to direct inversion approaches.

Through simulations for the FYST experiment, we evaluated how systematic and random errors affect the measurement accuracy and determined the optimal receiver-separation distance in the focal plane. In addition to these effects, atmospheric fluctuations might represent a dominant source of phase uncertainty in the FYST holography experiment. In this respect, the proposed method does not require the beam maps to be sampled on a strictly regular grid and does not require uniform coverage of the beam map. This flexibility allows for the scan trajectory to be optimized for more frequent beam-center calibration, while still maintaining high mapping efficiency. For instance, a daisy-like scan pattern (Ren et al. 2020, Sect. 4) may be used to provide frequent revisits to the beam center for calibration.

Both the full FYST simulations and the laboratory experiments show that the measurement error near the reflector edges is larger than that in the central region. To improve the measurement accuracy of the edge panels, additional off-axis beam measurements may be required so that these panels are more effectively illuminated and better constrained in the reconstruction. The FYST reflector surfaces will be measured using two independent systems: the proposed holography system and a laser metrology system. These two techniques provide complementary information and enable cross-validation of the reconstructed surfaces. In particular, the alignment of the edge panels is expected to rely more strongly on the laser-metrology measurements, which are not limited by the illumination pattern of the feed. The FYST near-field holography measurements are also restricted to a single telescope elevation because of the fixed source position and therefore cannot be used to characterize gravity-induced surface deformations as a function of elevation angle.

As part of this development, two efficient beam-simulation techniques, the two-step PO method and the two-step Fresnel-Kirchhoff diffraction method, were developed. Based on these methods, together with approximations for the phase changes of the fields on the reflectors and GPU acceleration, the beam calculations for given surface deviations can be completed within 0.1 s for five beam-map calculations without significant loss of accuracy. Although originally developed to support the fitting process, these methods also provide an efficient way to study the optical performance of CD telescopes with high precision.

Acknowledgements. The work was carried out at Universität zu Köln within the Collaborative Research Centre 956, sub-projects D2 and S, funded by the Deutsche Forschungsgemeinschaft (DFG) – project ID 184018867. The team at Universidad de Chile acknowledges the support from ANID through project QUIMAL 180004. X.R. acknowledges with gratitude the contributions of the late Richard E. Hills, whose support and guidance were instrumental to this work, and thanks the University of Iceland for support during the final preparation of the manuscript.

References

Baars, J. W. 2007, The Paraboloidal Reflector Antenna in Radio Astronomy and Communication (Springer), 348
Baars, J. W. M., Lucas, R., Mangum, J. G., & Lopez-Perez, J. A. 2007, IEEE Antennas and Propagation Magazine, 49, 24
Barrueto, I., Graf, U., Honingh, C., et al. 2022, in 12022 47th International Conference on Infrared, Millimeter and Terahertz Waves (IRMMW-THz), 1
Bennett, J., Anderson, A., McInnes, P., & Whitaker, A. 1976, IEEE Transactions on Antennas and Propagation, 24, 295
Bondo, T., & Sorensen, S. B. 2005, IEEE Transactions on Antennas and Propagation, 53, 1062
Born, M., Wolf, E., Bhatia, A. B., et al. 1999, Principles of Optics: Electromagnetic Theory of Propagation, Interference and Diffraction of Light, 7th edn. (Cambridge: Cambridge University Press)
Cassanelli, T., Bach, U., Winkel, B., & Kraus, A. 2024, A&A, 687, A27
CCAT-Prime Collaboration (Aravena, M., et al.) 2022, ApJS, 264, 7
Collin, R. E., & Zucker, F. J. 1969, Antenna Theory (USA: McGraw-Hill)
Dragone, C. 1978, Bell Syst. Tech. J., 57, 2663
Goodman, J. W. 2005, Introduction to Fourier Optics (Colorado: Roberts and Company publishers)
Hills, R., Dabrowski, Y., Gibson, H., et al. 2002, High-resolution millimetre-wave holography on the James Clerk Maxwell Telescope, URSI Assembly Maastricht
Milligan, T. A. 2005, Modern Antenna Design (Hoboken: John Wiley & Sons)
Morris, D., Baars, J. W. M., Hein, H., Steppe, H., & Thum, C. 1988, A&A, 203, 399
Niemack, M. D. 2016, Appl. Opt., 55, 1688
Nikolic, B., Hills, R. E., & Richer, J. S. 2007a, A&A, 465, 679
Nikolic, B., Prestage, R. M., Balser, D. S., Chandler, C. J., & Hills, R. E. 2007b, A&A, 465, 685
Niu, K., & Tian, C. 2022, J. Opt., 24, 123001
Nocedal, J., & Wright, S. J. 2006, Numerical Optimization (Berlin: Springer)
Oberst, T. E., Parshley, S. C., Stacey, G. J., et al. 2006, ApJ, 652, L125
Paknys, R. 2016, Applied Frequency-domain Electromagnetics (Hoboken: John Wiley & Sons)
Parshley, S. C., Kronshage, J., Blair, J., et al. 2018a, SPIE, 10700, 1744
Parshley, S. C., Niemack, M., Hills, R., et al. 2018b, SPIE, 10700, 1292
Paszke, A., Gross, S., Massa, F., et al. 2019, Advances in Neural Information Processing Systems (USA: NeurIPS), 32
Ramasawmy, J., Klaassen, P. D., Cicone, C., et al. 2022, SPIE Conf. Ser., 12190, 1219007
Ren, X., Astudillo, P., Graf, U. U., et al. 2020, SPIE, 11445, 1129
Rusch, W., & Potter, P. 2013, Analysis of Reflector Antennas (Cambridge: Academic Press)
Ruze, J. 1966, Proceedings of the IEEE, 54, 633
Scott, P. F., & Ryle, M. 1977, MNRAS, 178, 539
Silver, S. 1984, Microwave antenna theory and design (New York: McGRAW Hill Book Comp.)
Ufimtsev, P. Y. 2014, Fundamentals of the Physical Theory of Diffraction (Hoboken: John Wiley & Sons)
Yaghjian, A. 1986, IEEE Transactions on Antennas and Propagation, 34, 30

Appendix A: Configuration of the FYST holography system

FYST holography requires measuring five independent beam maps of the telescope, with the receiver placed at well-separated positions in the focal plane. Figure A.1 shows the reflector panel layout and the five receiver mounting locations: one at the focal-plane center on the optical axis, and four at the corners of a square. Based on the simulations in Sect. 4, the square side length is chosen to be 800 mm.

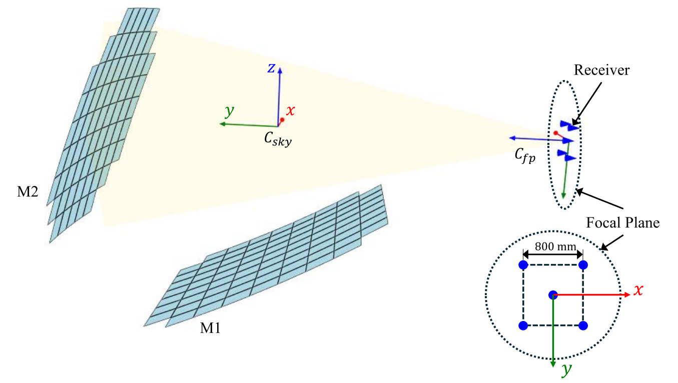

Fig. A.1. Schematic of the FYST holography optics. The figure shows the panel layouts of the primary (M1) and secondary (M2) reflectors of the FYST telescope. It also shows the five mounting positions of the 300 GHz holography receiver in the focal plane: one at the focal-plane center and four at (±400 mm, ±400 mm) relative to the focal-plane coordinate system, denoted by C_{fp}. The maximum separation between receiver positions is approximately 1130λ ($\lambda \approx 1$ mm at 300 GHz). C_{sky} denotes the coordinate system used for beam scanning.

Appendix B: Computational workflow of the two-step PO and two-step Fresnel–Kirchhoff methods

This appendix summarizes the computational implementation of the two-step PO method and the two-step scalar diffraction method used in this work. The physical propagation sequence has already been illustrated by the arrows in Fig. 4, and Fig. B.1 presents the corresponding computational workflow.

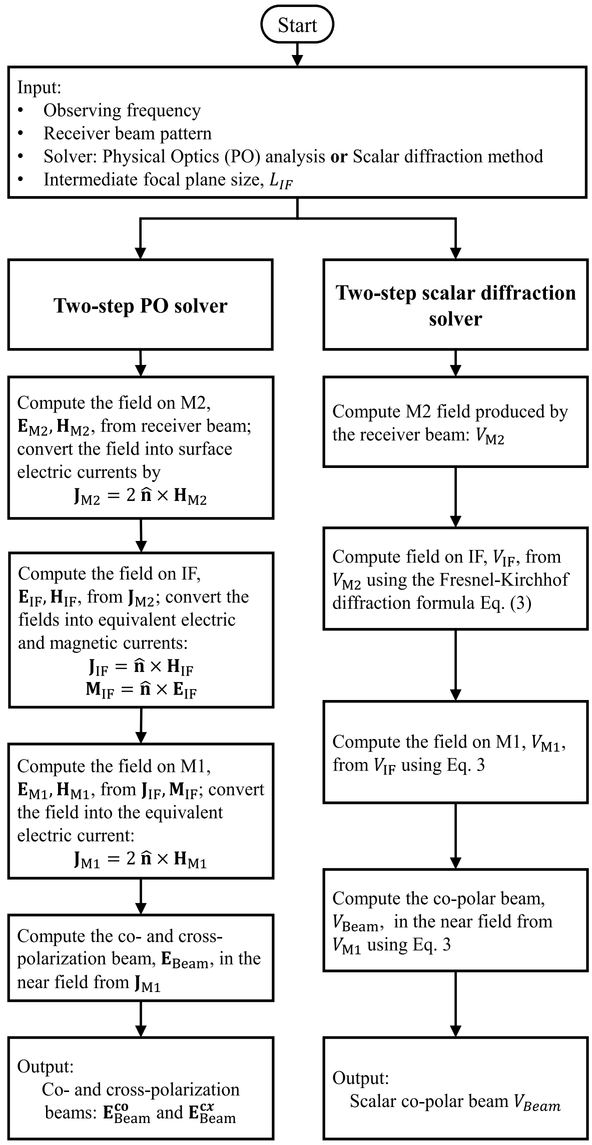

Fig. B.1. Flowchart of the computational implementation of the two-step PO method and the two-step scalar diffraction method. The diagram summarizes the main calculation steps for the two solvers, from the receiver beam to the near-field beam prediction. The corresponding physical wave-propagation sequence is illustrated in Fig. 4.

Appendix C: Construction of the accelerated beam prediction function for holographic analysis

This appendix summarizes how the beam prediction model is constructed as a function of the reflector surface deviations for the holographic analysis and outlines its computational workflow. For a given telescope geometry, receiver beam pattern, and receiver position in the focal plane, the telescope beam is evaluated through a sequence of field propagation from the receiver to M2, from M2 to the intermediate focal plane, from the intermediate focal plane to M1, and finally from M1 to the sky beam or the near-field region. The field propagation in each step is described by Fresnel–Kirchhoff diffraction formula, which, for a fixed propagation geometry, can be discretized into a matrix-form propagation operator, as discussed in Sect. 2.3. This appendix provides the detailed derivation and implementation of this accelerated beam prediction function, in which the reflector surface deviations are introduced as phase corrections to the sampled reflector surface fields.

As illustrated in Fig. C.1, we describe the imperfect reflector as the nominal surface S with a small normal displacement $\epsilon_S(q)$ at each sampled surface point q, which introduces an optical path change equal to $\epsilon_S(q)(\cos\theta_{\mathrm{in}} + \cos\theta_{\mathrm{out}})$. Under the small-perturbation approximation, the perturbed reflector is replaced by the nominal surface, and the effect of the surface error is retained only through the phase-correction factor. Applying the Eq. (3), the scattered field at point p can then be written as a function of the surface error ϵ_S:

$$V_T^p(\epsilon_S) \approx \iint_S K_{S\to T}\,(p,q)\; V_S^q\; C_S\,(\epsilon_S\,(q))\;\, dS\,, \tag{C.1}$$

where

$$K_{S\to T}\,(p,q) = \frac{i}{2\lambda}\,\frac{e^{ikr}}{r}\,\left(\cos\theta_{\mathrm{in}} + \cos\theta_{\mathrm{out}}\right), \tag{C.2}$$

$$C_S\,(\epsilon_S\,(q)) = \exp\Big[-ik\,\epsilon_S\,(q)\,\left(\cos\theta_{\mathrm{in}} + \cos\theta_{\mathrm{out}}\right)\Big]. \tag{C.3}$$

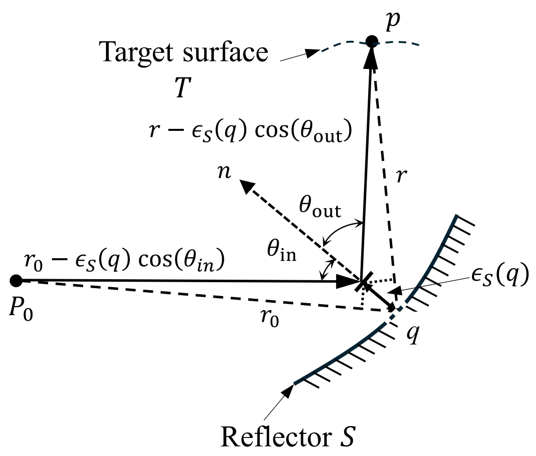

Fig. C.1. Same geometry as Fig. 7 but with a reflector deviation $\epsilon(q)$ applied at point q on the reflector surface S. The deviation is a normal displacement relative to the ideal surface, and it is incorporated in the Fresnel-Kirchhoff integral as a phase perturbation through the modified optical path length.

Here, $q = 1, 2, \ldots, N_S$ and $p = 1, 2, \ldots, N_T$ denote the indices of the sampled points on the reflector surface S and the observation points on the target surface T, respectively.

$C_S(\epsilon_S(q))$ represents the phase-correction factor applied to V_S^q to account for the reflector surface error at point q. In general, this factor depends on both the incident angle and the outgoing angles. For the FYST application, however, the variation in the outgoing angle is very small for propagation from M2 to the IF plane, and similarly for propagation from M1 to the source region. The outgoing angle can therefore be approximated as equal to the incident angle, so $C_S(\epsilon_S(q))$ depends only on the surface point q. Under this approximation, the phase-correction factor reduces to

$$C_S\left(\epsilon_S\left(q\right)\right) \approx \exp\Big[-i\, 2k\, \epsilon_S(q) \cos\theta_{\mathrm{in}}\Big]. \tag{C.4}$$

For the numerical implementation, we discretize the surface S into N_S samples $\{q\}$, and assign to each sample a surface element ΔS_q. The surface integral is then approximated by the following summation:

$$V_T^p(\epsilon_S) \approx \sum_{q=1}^{N_S} K_{S\to T}^{pq}\, V_S^q\, C_S\left(\epsilon_S(q)\right), \tag{C.5}$$

where

$$K_{S\to T}^{pq} \equiv K_{S\to T}\left(p, q\right) \Delta S_q. \tag{C.6}$$

The summation can be written in matrix form by collecting the sampled fields on S into the column vector $\mathbf{V}_S = \left[V_S^1, V_S^2, \ldots, V_S^{N_S}\right]^{\mathsf{T}}$, and the corresponding phase-correction factors into $\mathbf{C}_S\left(\epsilon_S\right) = \left[C_S\left(\epsilon_S\left(1\right)\right), C_S\left(\epsilon_S\left(2\right)\right), \ldots, C_S\left(\epsilon_S\left(N_S\right)\right)\right]^{\mathsf{T}}$. Likewise, the field samples on the target surface T are written as $\mathbf{V}_T\left(\epsilon_S\right) = \left[V_T^1, V_T^2, \ldots, V_T^{N_T}\right]^{\mathsf{T}}$. We define a matrix $\mathbf{K}_{S\to T}$ with entries $(\mathbf{K}_{S\to T})_{pq} = K_{S\to T}^{pq}$. In this notation, the dependence on the indices p and q is implicit, and the summation can be written compactly as

$$\mathbf{V}_T\left(\epsilon_S\right) \approx \mathbf{K}_{S\to T}\left(\mathbf{V}_S \odot \mathbf{C}_S\left(\epsilon_S\right)\right), \tag{C.7}$$

where $\odot$ denotes the element-wise product.

In the FYST implementation, the computational workflow can be expressed by the following three equations, evaluated in sequence:

$$\mathbf{V}_{\mathrm{IF}} = \mathbf{K}_{\mathrm{M2}\to\mathrm{IF}}\left(\mathbf{V}_{\mathrm{M2}} \odot \mathbf{C}_{\mathrm{M2}}\left(\epsilon_{\mathrm{M2}}\right)\right), \tag{C.8a}$$

$$\mathbf{V}_{\mathrm{M1}} = \mathbf{K}_{\mathrm{IF}\to\mathrm{M1}}\, \mathbf{V}_{\mathrm{IF}}, \tag{C.8b}$$

$$\mathbf{V}_{\mathrm{Beam}} = \mathbf{K}_{\mathrm{M1}\to\mathrm{Beam}}\left(\mathbf{V}_{\mathrm{M1}} \odot \mathbf{C}_{\mathrm{M1}}\left(\epsilon_{\mathrm{M1}}\right)\right), \tag{C.8c}$$

where $\mathbf{V}_{\mathrm{M2}}$, $\mathbf{V}_{\mathrm{IF}}$ and $\mathbf{V}_{\mathrm{M1}}$ denote the scalar field distributions on M2, IF plane and M1, respectively. The field in the source region corresponds to the telescope near-field beam map, and is denoted by $\mathbf{V}_{\mathrm{Beam}}$. ϵ_{M2} and ϵ_{M1} represent the surface error distributions on M2 and M1. The matrices in Eq. C.8 are independent of the surface errors and, thus, they only need to be computed once for the ideal reflector configuration and then stored for repeated use in subsequent evaluations. It is worth noting that for the propagation from M2 to the IF plane, the matrix $\mathbf{K}_{\mathrm{M2}\to\mathrm{IF}}$ is constructed using the reverse phase factor e^{-ikr} instead of e^{ikr}, since this step represents backward propagation to the intermediate focal plane.

Consequently, the beam simulation process is simplified to three matrix–vector multiplications, with the phase modification factors $\mathbf{C}_{\mathrm{M2}}$ and $\mathbf{C}_{\mathrm{M1}}$ introduced sequentially in the propagation steps associated with M2 and M1. No phase correction is required on the IF plane, as it serves only as an intermediate computational surface and does not introduce any surface error. The overall workflow for constructing the beam prediction function is illustrated in Fig. C.2.

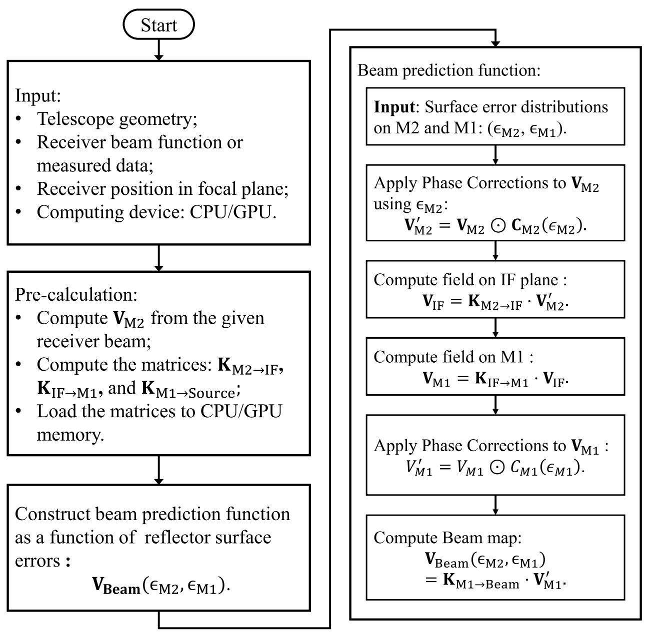

Fig. C.2. Flowchart illustrating the computational workflow of the beam prediction function used in the holographic analysis. The propagation matrices $\mathbf{K}_{\mathrm{M2}\to\mathrm{IF}}$, $\mathbf{K}_{\mathrm{IF}\to\mathrm{M1}}$ and $\mathbf{K}_{\mathrm{M1}\to\mathrm{Beam}}$ are precomputed and loaded into the memory of the selected device to accelerate the beam calculation. Reflector surface errors are incorporated through phase-correction factors applied on the M2 and M1 fields. $\mathbf{V}'_{\mathrm{M2}}$ and $\mathbf{V}'_{\mathrm{M1}}$ denote the fields on M2 and M1 after applying the phase correction factors $\mathbf{C}_{\mathrm{M1}}(\epsilon_{\mathrm{M1}})$ and $\mathbf{C}_{\mathrm{M2}}(\epsilon_{\mathrm{M2}})$, which are the reflector surface deviations ϵ_{M1} and ϵ_{M2}, respectively.

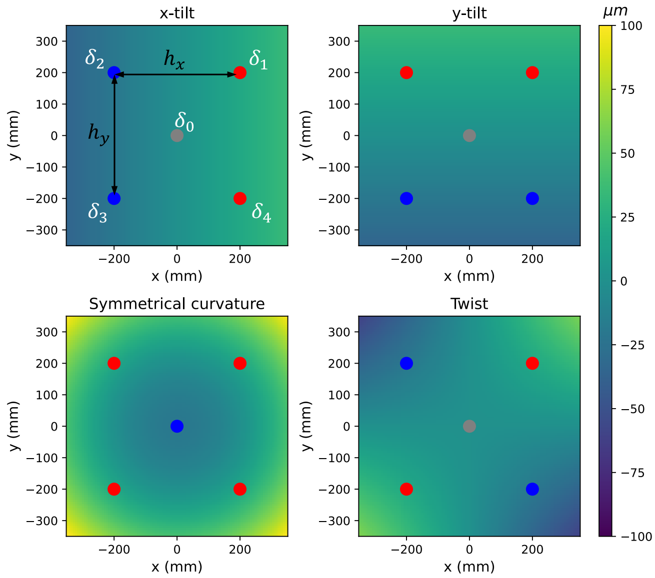

Fig. D.1. Panel distortion modes associated with the five-adjuster configuration: x-tilt, y-tilt, symmetrical curvature, and twist. The colored markers indicate the positions of the panel adjusters. h_x and h_y are the separations between the four corner adjusters in the x- and y-directions. δ_0, δ_1, δ_2, δ_3, and δ_4 are the displacement values of the five adjusters along the z-axis. The corresponding adjuster displacements with respect to the ideal positions are shown by the marker colors: red indicates an upward movement, blue a downward movement, and gray no movement.

Appendix D: FYST panel distortion modes induced by adjuster displacements

This appendix illustrates the panel distortion modes of the FYST telescope induced by adjuster displacements. Each panel is supported by five z-axis adjusters with displacements denoted by δ_0, δ_1, δ_2, δ_3, and δ_4 (Fig. D.1), including one at the panel center and four at the corners of a rectangle with side length h_x and h_y. For small deformations, the panel surface error is modeled by the second-order polynomial in Eq. 4 and can be decomposed into five distortion modes: piston, x-tilt, y-tilt, symmetric curvature, and twist. Figure D.1 shows that the calculation of Eq. 4 at the five adjuster locations yields a linear mapping between the polynomial coefficients and δ_{0-4}, which allows the panel deformation to be expressed directly in terms of the adjuster displacements, as given by

$$a_0 = \delta_0 \tag{D.1}$$

$$a_1 = \frac{\delta_1 - \delta_2 - \delta_3 + \delta_4}{2\,h_x}, \tag{D.2}$$

$$a_2 = \frac{\delta_1 + \delta_2 - \delta_3 - \delta_4}{2\,h_y}, \tag{D.3}$$

$$a_3 = \frac{\delta_1 - \delta_2 + \delta_3 - \delta_4}{h_x\,h_y}, \tag{D.4}$$

$$a_4 = \frac{\delta_1 + \delta_2 + \delta_3 + \delta_4 - 4\,\delta_0}{h_x^2 + h_y^2}. \tag{D.5}$$